

# A 22 V Compliant 56 $\mu$ W Twin-Track Active Charge Balancing Enabling 100% Charge Compensation Even in Monophasic and 36% Amplitude Correction in Biphasic Neural Stimulators

Natalie Butz<sup>ID</sup>, Student Member, IEEE, Armin Taschwer<sup>ID</sup>, Member, IEEE,  
 Sebastian Nessler<sup>ID</sup>, Student Member, IEEE, Yiannos Manoli, Senior Member, IEEE,  
 and Matthias Kuhl, Member, IEEE

**Abstract**—Closed-loop charge balancers make a considerable contribution to a safe and secure electrical stimulation and additionally present an alternative to bulky blocking capacitors. This CMOS-integrated, 22 V compliant Twin-Track active charge balancer accomplishes both instantaneous and long-term balanced conditions. Long-term charge balancing is achieved by a cause-based PI-controlled offset compensation of the remaining electrode voltage. A  $G_m$  of only 1.5 nS offers a large (8 ms) time constant with only a 12 pF capacitor and leads to the first integrated PI-controller for offset compensation in neural implants. Instantaneous autonomous balancing is realized by a second concept, the consequence-based Inter-Pulse Charge Control. It uses a class-B architecture to supply the compensation currents. Thus, no additional references are required to define the safety window of the remaining electrode voltage. It consumes 31.8  $\mu$ W in the idle state, while the delivered output power can be as high as 11 mW. The two complementary approaches can be combined to one system, providing the opportunity to achieve a better performance. The system consumes 56  $\mu$ W and features a 36% mismatch correction in biphasic stimuli amplitude, as well as an autonomous 100% charge removal at maximum compensation amplitudes of 500  $\mu$ A, which makes it a suitable complement to monophasic stimulators.

Manuscript received June 16, 2017; revised February 5, 2018; accepted April 8, 2018. Date of publication May 18, 2018; date of current version July 20, 2018. This paper was approved by Associate Editor Michiel A. P. Pertjjs. This work was supported in part by the German Research Foundation (DFG) under Grant MA 2193/20-1 and in part by the BrainLinks-BrainTools Cluster of Excellence (DFG) under Grant EXC 1086. (*Corresponding author: Natalie Butz.*)

N. Butz and S. Nessler are with the Fritz Huettinger Chair of Microelectronics, Department of Microsystems Engineering – IMTEK, University of Freiburg, 79110 Freiburg, Germany (e-mail: natalie.butz@imtek.de).

A. Taschwer is with Hahn-Schickard, 78052 Villingen-Schwenningen, Germany.

Y. Manoli is with the Fritz Huettinger Chair of Microelectronics, Department of Microsystems Engineering – IMTEK, University of Freiburg, 79110 Freiburg, Germany, also with Hahn-Schickard, 78052 Villingen-Schwenningen, Germany, and also with the BrainLinks-BrainTools Cluster of Excellence, 79110 Freiburg, Germany.

M. Kuhl was with the Fritz Huettinger Chair of Microelectronics, Department of Microsystems Engineering – IMTEK, University of Freiburg, 79110 Freiburg, Germany, and also with the BrainLinks-BrainTools Cluster of Excellence, 79110 Freiburg, Germany. He is now with the Institute of Integrated Circuits, Hamburg University of Technology (TUHH), 21073 Hamburg, Germany.

Color versions of one or more of the figures in this paper are available online at <http://ieeexplore.ieee.org>.

Digital Object Identifier 10.1109/JSSC.2018.2828823

**Index Terms**—Active charge balancing (CB), blocking capacitor, class B, CMOS, functional electrical stimulation (FES),  $G_m$  cell, high-voltage (HV) compliance, long-term implant, neural stimulator, PI controller.

## I. INTRODUCTION

FUNCTIONAL electrical stimulation (FES) is a technique that allows the stimulation of nerves by electrical charge to treat a variety of diseases and disorders. Beside cardiac pacemakers, impressive success is achieved with cochlear implants and retinal prosthesis to restore hearing and visual perception [1], [2]. Deep brain stimulators to treat several types of neurological dysfunctions, like Parkinson's disease, and vagus nerve stimulation (VNS) to treat severe epilepsy [3], [4] are therapy methods that use FES. A novel approach to overcome chronic hypertension is selective VNS by BaroLoop [4]. At the event of a too high blood pressure, e.g., caused by altered stiffness of arterial wall, the strength of the afferent nervous signals is reduced. The solution is to override the vagal signal with the help of artificial electrical stimulation. However, the transfer of blood pressure information to the brain is only one of the vagus nerve's functions. The inadvertent stimulation of non-baroreceptive fibers may cause severe side effects like bradycardia and bradypnea [5]. Therefore, BaroLoop aims to localize the relevant fibers and extracts blood pressure information by tripolar recording [6] via a cuff electrode [5], which is wrapped around the vagus nerve as shown in Fig. 1 left. The localized electrode triole is then used for selective stimulation.

Using biphasic current pulses for stimulation, the main transferred charge is compensated by reversing the current direction. However, due to imperfections in the fabrication process of integrated circuits, mismatch in the biphasic waveform always occurs. In order to avoid charge accumulation, which causes tissue lesion and electrode corrosion, in particular during long-term treatments, charge balancing (CB) has become an integral part of FES [9]. However, for reliability reasons, most certified medical devices are equipped with DC-blocking capacitors or passive CB systems, despite their disadvantage in size, long settling times, and uncontrolled

charge compensation. A promising approach to small, fast, and well-controlled charge compensation is active CB. This paper presents a CMOS-integrated Twin-Track active charge balancer, accomplishing “cause and consequence”-based compensation, for long-term as well as instantaneous balanced conditions. The Twin-Track system reduces the hazards of electrical stimulation, facilitates safe chronic trials, and thus introduces an alternative to blocking capacitors.

Beside the important safety aspect of CB in neural stimulation, this paper also aims at solving the challenges of a novel approach of Dr. Plachta’s group [5]. The idea is to equip the stimulator setup with the capability to influence the direction of the applied stimulus via steering currents. These steering currents originating at neighboring stimulation sites are used to either fine tune the applied current for an improved efficacy or to block the spreading of activity in unwanted directions using anodal blocks. Fig. 1 shows the principle of steering currents with 30 versus 500  $\mu$ A stimulation currents. The steering electrode is located at the opposing stimulation site in order to focus the electrical field deeper within the nerve. The stimulus amplitude at the main stimulation electrode, the cathode, is predefined precisely by recording its effect on the actual blood pressure. A biphasic counter pulse is programmed to compensate most of the remaining charges. However, for precise long-term charge compensation, a background operation in the form of an analog CB is desired, allowing to use the same electrode for an intermediate neural recording, without risking digital signal interference. The more electrodes are active on the perimeter of the cuff to steer the electrical field, the higher is the probability of crosstalk from adjacent electrodes, leading to charge redistribution. Therefore, preprogrammed biphasic counter pulses for CB are not suitable for these electrodes. This paper presents the first charge balancer that is capable of generating counter pulses autonomously, without programming, but still with self-adaptive timing, to balance the charges of monophasic steering and anodic counter currents. The simulation results present in Fig. 1 (bottom right) show the distribution of the electrical field lines during stimulation, including steering currents. The lines expand even beyond the anodal rings, causing charge redistribution at neighboring sites. Therefore, it is of interest to place additional standalone CB systems, in some distance apart from the actual stimulation site to block the spreading of activity in unwanted directions while stimulating.

The Twin-Track system consists of a closed-loop balancer for an analog background operation as well as a self-adaptive balancer for automatic counter pulse generation that can be used in combination or as a standalone implementation. The user-friendly standalone function has the merit of complementing already certified stimulation systems and reducing the programming and circuit overhead, since it works autonomously and independent of the stimulator unit. In addition to the requirements of implantable systems, such as low power consumption, the diversity of applications demands high adaptability and flexibility of the CB system implemented in terms of configurable safety window, limitation of compensation currents, and high-voltage (HV) compatibility. Furthermore,

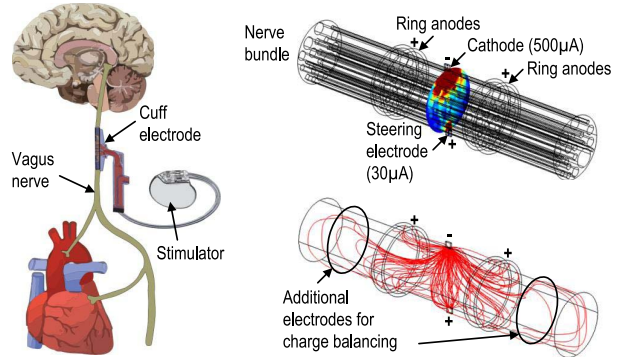


Fig. 1. Left: VNS for blood pressure control by BaroLoop [7]. Right: simulation of electrical field when using steering currents for an excitation of deeper nerve areas [8].

several controller options are available to adapt to different electrode impedances, for which a detailed closed-loop stability analysis is presented.

This paper is organized as follows. Section II introduces the stimulation setup, identifying the significance of CB. Section III explains the limited protection of blocking capacitors. Furthermore, the state-of-the-art charge balancers are classified into cause- and consequence-based methods. In Section IV, the architectures and measured characteristics of the developed charge balancers (Inter-Pulse Charge Control (IPCC) and PI-Controlled Offset Compensation (OC)) are presented, followed by the stability analysis of the PI-control loop. Section V presents the Twin-Track system measurements, using an equivalent electrode model as well as an *in vitro* electrode.

## II. SYSTEM OVERVIEW

The three stimulation methods for neural excitation are voltage, charge, and current mode stimulation, which are physically linked but describe the different approaches, i.e., controlled by a voltage source, capacitive discharge, or a current source [10]. However, it is the charge that has to be controlled, since the electrode-electrolyte interface is characterized by a maximum allowed charge that can be transferred from the electrode into the biological tissue. Taking into account that the load impedance varies over time, the injected charge differs when using voltage-controlled stimulators, which is why they are rarely used in modern implantable systems [1], [11]. Using charge-controlled stimulation via capacitive discharge, the stimulation charge is accurately controlled [10], [12], but in the case of high-load capacitances, large capacitors are required for sufficient charge delivery, which is not suitable for implantable systems. Furthermore, the waveform of the applied charge is predefined by the discharge characteristic and offers little flexibility. Current-controlled stimulation, in which pulsewidth  $t_{pw}$  and current amplitude are controlled regardless of impedance variations, is most commonly used [1], [11] as charge and current are directly linked. The conceptual configuration of the stimulation setup is shown in Fig. 2. The current-controlled stimulator releases biphasic pulses onto the electrode according to the digital control signal  $C_{ctrl}$ .

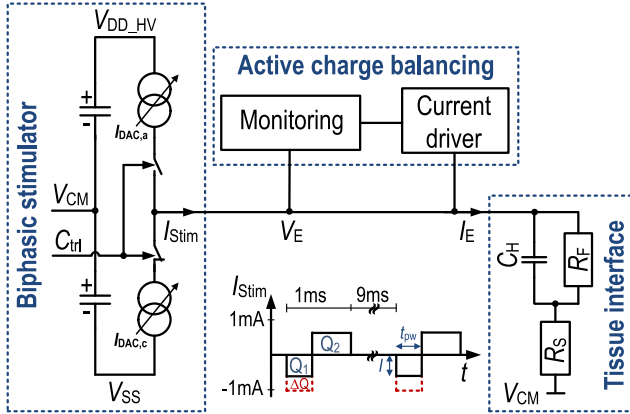


Fig. 2. System overview of the biphasic current-controlled neural stimulator, active CB, and the electrical equivalent model of the electrode–electrolyte tissue interface.

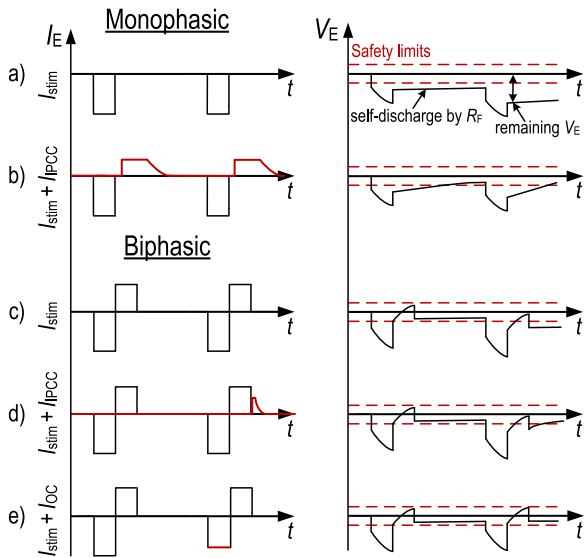


Fig. 3. Monophasic and imbalanced biphasic current pulses  $I_{Stim}$  (left) and the corresponding electrode voltage  $V_E$  (right) with respect to  $V_{CM}$ . (a) and (c) Rise of a remaining voltage  $V_E$ . (b) and (d) IPCC will compensate the remaining voltage in both monophasic and biphasic stimulation by introducing a compensation current. (e)  $O_C$  compensates biphasic mismatch by adjusting the amplitude of the stimulation pulse.

Different current waveforms are possible for successful stimulation as analyzed by [13]. However, the shape of waveform is irrelevant for the success of CB. Since the focus of this paper lies on active CB, only monophasic and biphasic pulses are considered (Fig. 3(a) and (c)). Monophasic stimulation consists of a negative (cathodic) stimulation pulse that depolarizes the nerve and thereby evokes the desired physiological effect. The more common biphasic current pulse consists of a cathodic stimulating phase and an anodic counter phase, reversing the electrochemical reactions by a stimulus of opposite sign [14].

During FES, the electrode is in direct contact with biological tissue, presenting the interface between stimulator circuitry and electrolyte in the body. A charge conversion from electron conduction in solid state to ion conduction in the fluid state takes place, which results in three main mechanisms:

capacitive, electrochemical, and redox reactions [15]. Based on these mechanisms, an electrical equivalent model, shown in Fig. 2, is derived, in which  $C_H$  represents the Helmholtz double-layer capacitor,  $R_S$  is the solution spreading resistance, and  $R_F$  the Faradaic resistance, which leads to reversible but also irreversible reactions. Especially, the latter is the source of toxicity in the case of a prolonged non-balanced condition of the electrode voltage  $V_E$  [15]. The electrode values vary depending on the material and geometry [16]. The complex impedance

$$Z_E(s) = (R_F + R_S) \frac{1 + sC_H \frac{R_S R_F}{R_S + R_F}}{1 + sC_H R_F} \quad (1)$$

describes the current–voltage behavior with respect to the frequency at the phase boundary.

One target of the balancer presented is to be adaptive to arbitrary stimulators and different applications, e.g., steering currents. Considering current amplitudes up to  $\pm 5$  mA and electrode impedances typically larger than  $1\text{ k}\Omega$  [1], HV-compliant systems are necessary. The supplies of the used stimulator are generated with respect to the body's quiescent potential  $V_{CM}$  and lie in the HV range (Fig. 2). To accommodate the variability in electrode impedance and patient threshold, it can be stated that a higher compliance voltage of the stimulator, and therefore also of the CB system, will offer a broader usability. Therefore, in contrast to [10] and [17], this paper features 22 V compliance ( $\pm 11$  V with respect to  $V_{CM}$ ), limited by the used  $0.35\text{ }\mu\text{m}$  HV CMOS process.

### III. CHARGE BALANCING CONCEPTS

A first approach for tissue and electrode protection is using biphasic instead of a monophasic stimulation pulse. During biphasic stimulation, the electrochemical reactions are reversed and the transferred charges are ideally compensated directly within the second phase. However, a mismatch in the biphasic waveform ( $\Delta Q$  in Fig. 2) inevitably occurs due to process variations. Residual net charges lead to irreversible Faradaic reactions with toxic byproducts causing pH changes and electrode dissolution [15]. Therefore, any residual charge at the electrode–electrolyte tissue interface must be monitored and compensated. A measure is the remaining electrode voltage  $V_E$ . Any monophasic or unbalanced biphasic stimulus  $I_{Stim}$  (Fig. 3(a) and (c)) causes a consecutive rise of remaining  $V_E$ . With respect to the application and electrode material, a safety voltage window is defined, in which  $V_E$  is tolerable [14]. At this point, charge balancing becomes indispensable, as it keeps  $V_E$  within these predefined safety limits (Fig. 3(b), (d), and (e)).

#### A. Replacing Blocking Capacitors

Introducing a blocking capacitor  $C_{block}$  in series to the electrode (Fig. 4) is often argued [14], [18], [19] to protect the tissue against net currents. Maximum allowed net currents are defined in [20], being determined by observing tissue damage and relating it to an overall net current. However, the influence of the electrode impedance, e.g., the amount of charge accumulation and the capability of self-discharge,

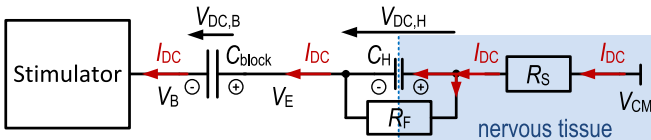


Fig. 4. Effect of a blocking capacitor  $C_{block}$  for DC currents and the critical development of voltages  $V_{DC,H}$  and  $V_{DC,B}$ .

is neglected. Therefore, the derived current limits are not universally valid; on the contrary, they vary considerably from one application to another.

During voltage mode stimulation,  $C_{block}$  isolates the DC level of  $V_E$  from  $V_B$  on the circuitry side. Therefore, a self-discharge at the electrode via  $R_F$  can take place until  $V_E$  equals  $V_{CM}$ . Nevertheless, fast switching events and AC voltages (e.g., stimulation pulses) will pass  $C_{block}$  and may lead to a residual voltage  $V_{DC,H}$  across  $C_H$  (Fig. 4). Considering current mode stimulation, any DC and AC current, e.g., stimulation and erroneous DC offset currents, is being integrated at  $C_{block}$  and  $C_H$ , thereby mobilizing ions in the tissue that accumulate at the phase boundary. Therefore, introducing a blocking capacitance will not protect the electrode from the development of a residual voltage  $V_{DC,H}$ . Only in the case of a permanent offset current, blocking capacitors are reasonable, since they interrupt the integration process at  $C_H$  as soon as a constant voltage  $V_B$ , e.g., the supply due to clipping of the stimulator, is reached, allowing for a self-discharge of  $V_{DC,H}$ . Furthermore, during stimulation, a voltage drop across  $C_{block}$  is induced, thus increasing the voltage overhead required for successful stimulation. Therefore,  $C_{block}$  must be chosen significantly larger than  $C_H$  to result in a voltage drop that is negligible compared to that across  $C_H$  [14]. Blocking capacitances are expected in the range of 1–100  $\mu$ F and have to be realized off chip, bringing along disadvantages in terms of area and assembly.

Even though using blocking capacitors is an accepted method, and practiced in many stimulators, it can be stated that  $C_{block}$  has disadvantages in terms of area and effectiveness. It is neither a sufficient protection nor an alternative to CB in current mode stimulators.

#### B. “Cause and Consequence”-Based Compensation Methods

In this paper, we distinguish between consequence- and cause-based methods, since they differ in their mode of compensation. The consequence-based approach aims for an instantaneous reduction of  $V_E$  above the safety limit, after each stimulus. Cause-based methods try to adjust the charges of the anodic and cathodic stimulus, typically averaged over many pulses, ensuring long-term balanced conditions. Cause-based compensation is suitable for counteracting mismatch and process variations, but might show a settling process with overshoots during startup.

One subgroup of the *consequence-based compensation* methods is passive CB, such as electrode shortening by discharge resistors [2], [3], [14]. However, its success and compensation current intensities are not controlled. They depend on the amount of residual charge, the time available for

discharge, and its time constant, defined by the electrode impedance and discharge resistance [14], [21]. In addition, several electrodes shorted simultaneously to  $V_{CM}$  distribute their charges among each other in an uncontrolled manner, in which current peaks might trigger action potentials.

The second subgroup is active consequence compensation, e.g., by short pulse injection of a fixed amount of charge [1], [9], [10], [22]. However, the ensuing possibility of “[...] an unwanted neural stimulation has not been proven yet. [...] the maximum amount of mismatch charge, which can be compensated, depends on the adjusted charge per pulse and the number of pulses allowed over time” [9]. Additional control units or components, e.g., comparators, are necessary to estimate the charge packages and determine the safety window and pulse polarity. Charge estimation or calculation makes this method not suitable for applications that require real-time monitoring of  $V_E$  for fast charge removal. Furthermore, the current source is incorporated in the stimulator design, sharing its hardware (front end). Thus, an application as stand-alone balancer, as a complement to monophasic stimulators, with continuous current supply for counter pulse generation is not possible. The short pulse injection method is stable only if the time between two stimuli is long enough to fit the required number of balancing pulses and the charge of these pulses is small enough to not exceed the safety window, which might otherwise result in toggling. High switching events will not only be harmful when exciting low-volume neural tissue, but are also a source of noise, causing unwanted blanking of neural events during recording. Therefore, going from the digital pulse insertion to an analog continuous balancing significantly reduces the number of high-frequency switching events seen by the tissue.

The aim of all *cause-based compensation* methods is to adjust the cathodic and anodic stimulation pulses by means of amplitude or pulselength correction. In essence, however, they differ in their reference that is used for successful compensation. The first subgroup [3], [16], [17], [23] adjusts the biphasic stimulation pulse based on the surveillance of the transferred charges. But even with perfectly matched cathodic and anodic current charges, a zero residual charge at the electrode will not be achieved, due to the disturbances on the electrode voltage, e.g., by crosstalk of adjacent electrodes, and self-discharge during inter-pulse delays [21]. Furthermore, electrochemical processes at the phase boundary differ for positive and negative charges, which causes an additional kind of charge leakage.

In contrast, the second cause-based subgroup adjusts the biphasic stimulation pulse by monitoring  $V_E$  [1], [9], [21], [24]. Thus, all the above-mentioned changes, disturbances, and processes at the electrode-electrolyte interface are automatically incorporated. Such a charge balancing operation is known as OC [9]. According to the actual charge imbalance, compensating charges are continuously supplied as an offset current in the background. It takes an initial settling process to adjust the offset current to balance the biphasic stimulation pulses and works well in continuous systems for chronic implantation. However, OC balancers must provide an integration time constant larger than the stimulation period

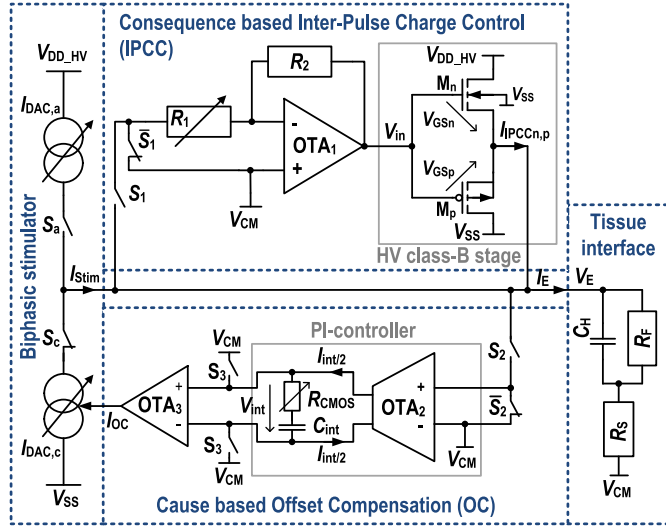


Fig. 5. Presented concept of the cause and consequence-based Twin-Track active charge balancer.

to ensure a memorylike behavior of the offset value over multiple stimulation pulses. Thus, the time constant must be in the order of a few milliseconds, requiring large  $RC$  values, which are realized on a printed circuit board (PCB) using discrete components in [9]. Therefore, the proposed application specific integrated circuit (ASIC) implementation in [1] exchanges the continuous-time integrator of [9] with a 3-bit Moore state machine to control the additional offset current, according to an HV window comparator. The digital OC is limited by the total amount of compensation charges and by its precision according to the number of bits. The analog OC balancer presented here is an ASIC implementation, using a  $G_m$  approach for realistic  $RC$ -value substitute. In addition, in contrast to [9] and [25], this paper recommends a configurable PI-control, introducing an additional zero that is adaptive to different electrodes and therefore beneficial in terms of stability.

#### IV. CIRCUIT IMPLEMENTATION AND CHARACTERIZATION

This paper presents the cause and consequence Twin-Track charge balancing system, as shown in Fig. 5. Both controls are based on the real-time monitoring of  $V_E$ . The consequence-based system is named Inter-Pulse Charge Control (IPCC) due to its instantaneous compensation properties between the stimulations. The cause-based system is named PI-controlled Offset Compensation (OC), since it corrects the negative stimulus amplitude to reach a charge-compensated state. Both charge balancers can be activated independently via  $S_1$  and  $S_2$ , the OC is reset when needed by discharging  $C_{int}$  via  $S_3$ . The signal flow in Fig. 6 shows the timing diagram with respect to the stimulation pulses. Directly after each stimulus,  $S_2$  is high for an interval of 300  $\mu$ s to measure  $V_E$ , the corresponding mismatch value is stored on  $C_{int}$ . Subsequently,  $S_1$  turns high and the IPCC starts monitoring  $V_E$ , balancing the remaining charges instantaneously.  $S_1$  stays high until the next stimulus starts, thus being able to

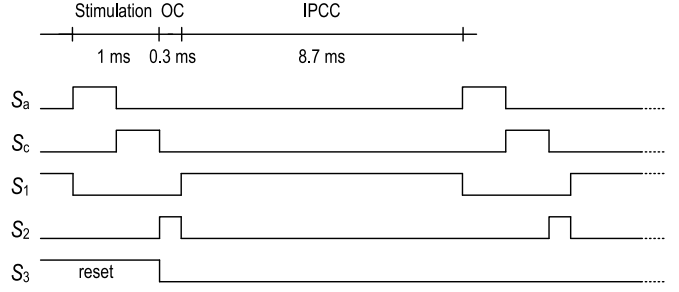


Fig. 6. Signal flow diagram, showing the timing of the Twin-Track active charge balancing system.

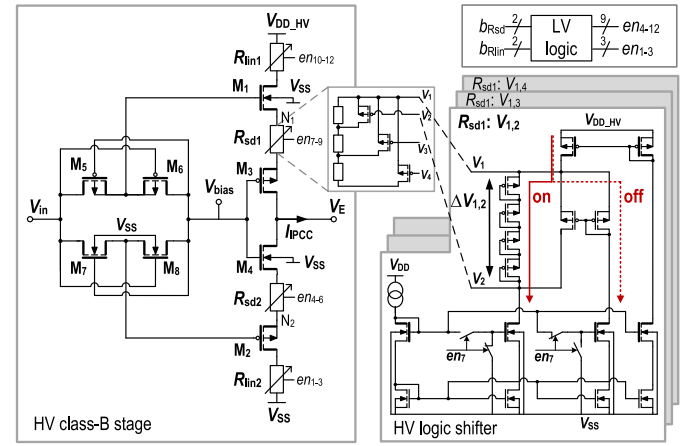


Fig. 7. Schematic of the implemented HV class-B stage including current limiting resistors  $R_{sd1,2}$  and  $R_{lin1,2}$ , as well as the HV logic shifter, exemplarily shown for  $R_{sd1}$ .

react to disturbances. However, the IPCC becomes inactive autonomously, usually before the next stimulus, once  $V_E$  has reached the safety window. Due to the HV environment, HV switches analog to the HV logic shifter introduced in Fig. 7 are implemented for  $S_1$  and  $S_2$ . Thus, presenting a solution for the lack in HV switches that is mentioned in [11] and [14]. Before explaining the combination of the CB circuits to the Twin-Track system, the description of each CB system is given separately. Therefore, an equivalent electrode model with the smallest expected capacitance ( $C_H$  of 0.1  $\mu$ F) for a polyimide thin-film cuff electrode [5] is chosen, thus depicting the largest CB effect.

##### A. Characteristics of the Inter-Pulse Charge Control

The IPCC monitors  $V_E$  with an HV-compliant inverting amplifier (OTA1) that steers an HV class-B stage, representing the compensating current source (Fig. 5). The main advantage of the presented IPCC is its instantaneous effectiveness with an overall simple design, as additional voltage references are dispensable in contrast to, e.g., [1], [9], [10], and [21]. The safety window  $\Delta V_{safe}$  is autonomously defined by the inherent hysteresis (dead zone) of the class-B stage, in which it stays inactive and consumes no power.  $\Delta V_{safe}$  is defined by

$$\Delta V_{safe} \leq \frac{R_1}{R_2} \cdot (|V_{tp}| + V_{tn}) \quad (2)$$

where  $V_{t_{n,p}}$  are the threshold voltages of transistors  $M_{n,p}$  (Fig. 5). The safety window can be configured to either  $\pm 50$  mV [10] or  $\pm 100$  mV [1] by trimming  $R_1$ . The output current  $I_{IPCCn,p}$  quadratically increases with effective gate-source voltage ( $|V_{GSn,p}| = |V_{in}| + |V_E|$ )

$$I_{IPCCn,p} = \frac{\beta_{n,p}}{2} \cdot \left( |V_E| \cdot \left( \frac{R_2}{R_1} + 1 \right) - |V_{t_{n,p}}| \right)^2. \quad (3)$$

Thus,  $I_{IPCC}$  has its highest amplitude right after a stimulus and decreases with ongoing compensation, making the best use of the refractory period of the nerve to achieve fast settling without risking the nerve's restimulation. The current through  $R_1$ , provided by  $OTA_1$ , additionally decreases  $V_E$ , but is negligibly small compared with the compensation current  $I_{IPCC}$  of up to  $\pm 500$   $\mu$ A. The ability for real-time monitoring of  $V_E$  with simultaneous charge compensation is especially advantageous at higher stimulation frequencies, since it allows for a faster charge balancing compared with current-free measurements that interrupt the compensation process.

The HV transistors of the used 0.35  $\mu$ m HV CMOS process can withstand a maximum  $V_{GS}$  of 18 V and a maximum gate-bulk voltage  $V_{GB}$  of 22 V. Therefore, a basic class-B architecture, as shown in Fig. 5, could be implemented for applications of up to 18 V supply only. However, to make full use of the maximum allowed  $V_{GB}$  headroom, an advanced class-B stage, with  $M_{1,2}$  as basic transistors, is introduced in Fig. 7. In the following,  $R_{lin1,2}$  and  $R_{sd1,2}$  may not be considered yet. The 22 V compliance is reached by two precautions. First, a gate protection technique ( $M_{5-8}$ ) is used, keeping  $V_G$  of  $M_{1,2}$  at  $V_{bias}$ , which is close to half the supply, during their inactive phase. Second, implementing transistors  $M_{3,4}$  shields the source nodes  $N_{1,2}$  from direct  $V_E$  variations. Since  $V_{in}$  changes proportionally with  $V_E$ , the output current  $I_{IPCC}$  still changes quadratically with  $V_E$  defined by

$$I_{IPCC} = \frac{k}{2} \cdot \left( |V_E| \cdot \frac{R_2}{R_1} - (V_{t1,4} + |V_{t3,2}|) \right)^2 \quad (4)$$

with

$$k = \beta_{1,3} \cdot \beta_{2,4} \cdot \frac{(\sqrt{\beta_{1,3}} \pm \sqrt{\beta_{2,4}})^2}{(\beta_{1,3} - \beta_{2,4})^2}. \quad (5)$$

The unsymmetrical bulk connections of the HV nMOS and pMOS transistors result in an unsymmetrical threshold range. To symmetrize the activation threshold of the upper and lower class-B stages around  $V_{CM}$ ,  $V_{bias}$  is slightly adjusted according to

$$V_{bias} = V_{CM} - \frac{(V_{t1} + |V_{t3}|) - (|V_{t2}| + V_{t4}))}{2}. \quad (6)$$

For charge compensation, a flat slope and low compensation amplitudes are preferred, since both influence the sensitivity of neurons to trigger action potentials [26]. Two methods for varying the slope and maximum amplitude of  $I_{IPCC}$  are implemented (Fig. 7): the current intensity can be limited either by increasing a resistance  $R_{sd1,2}$ , inducing source degeneration, or by increasing  $R_{lin1,2}$  forcing  $M_{1,2}$  earlier into the linear region. The maximum compensation amplitude is configurable to predefined limits between  $\pm 150$  and  $\pm 500$   $\mu$ A by a 2-bit

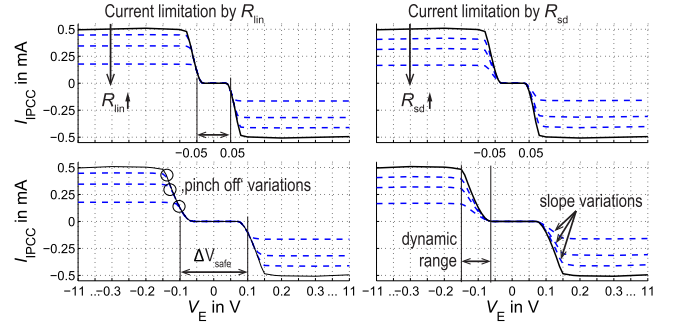


Fig. 8. Measured characteristics of the IPCC with a safety window of  $\pm 50$  mV in the top and  $\pm 100$  mV in the bottom graphs, showing the influence on  $I_{IPCC}$  when increasing  $R_{lin}$  (left) and  $R_{sd}$  (right).

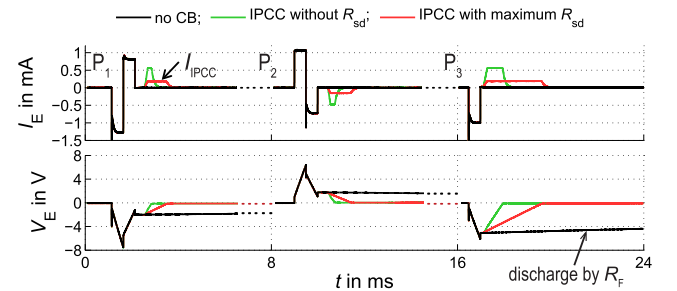


Fig. 9. Measured system results of the IPCC for compensation currents  $I_{IPCC}$  limited to around  $\pm 500$   $\mu$ A (green line) and to around  $\pm 150$   $\mu$ A (red line), using an electrode equivalent model with  $C_H$  of 0.1  $\mu$ F,  $R_F$  of 500 k $\Omega$ , and  $R_S$  of 1 k $\Omega$ .

low-voltage (LV) signal  $b_{Rsd}$  and  $b_{Rlin}$ , respectively. Each resistor consists of three subresistances, as shown exemplary for  $R_{sd1}$ . Beside  $R_{lin2}$ , all resistors are exposed to an HV environment. Thus, an HV logic shifter is required for shifting the LV digital control signal  $en_{4-12}$  into the HV domain. In the ON condition, a current of 10 nA is directed through a series of diode-connected transistors, providing a sufficient  $\Delta V_{1,2}$  to open the switching transistor, thus shortening one subresistance. In the OFF state, the same 10 nA are being directed through the second branch, actively pulling  $V_1$  toward  $V_2$  via the parallel current mirror configuration, closing the switching transistor.

The measured characteristics of  $I_{IPCC}$  are shown in Fig. 8. Within the dead zone of the IPCC, no current is released onto the electrode. In Monte Carlo simulation, the mean of the dead zone corresponding to the safety window of  $\pm 100$  mV is  $\pm 70$  mV around  $V_{CM}$  with  $\sigma$  uncertainty below 5.2 mV. Once this limit is exceeded, the current increases quadratically. The drain current induced voltage drop over  $R_{lin}$  decreases the dynamic range and limits the maximum output current. In contrast, increasing  $R_{sd}$  limits the current by flattening the output slope of  $I_{IPCC}$ , while keeping the dynamic range constant. With  $OTA_1$  being the only main active device in the monitoring state, the IPCC consumes 37.1  $\mu$ W (Table I), however, being capable of delivering an output power as high as 11 mW when needed.

The measured CB response of the IPCC is presented for two different current limits (Fig. 9). The stimulation pulse P1

TABLE I  
POWER CONSUMPTION OF THE TWO CHARGE-BALANCING CIRCUITS IN THEIR MONITORING STATE, LISTED BY COMPONENTS

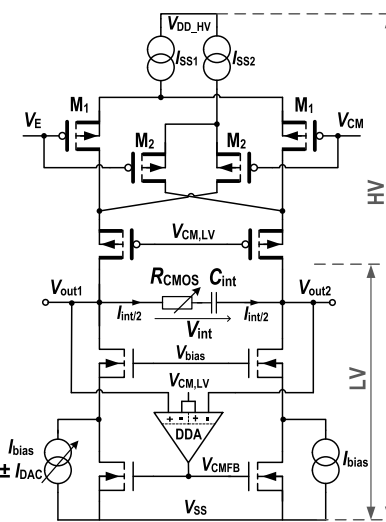
Components	IPCC			PI-controlled OC			
	OTA <sub>1</sub>	Class-B stage	HV logic shifter & $S_1$	OTA <sub>2</sub>	OTA <sub>3</sub>	$R_{CMOS}$	CMFB DDA
Simulated current	1.22 $\mu$ A	0 A	11 · 10 nA	610 nA	240 nA	80 - 640 nA	220 nA
Voltage	22 V	22 V	22 V	22 V	3 V	3 V	3 V
Simulated power		34.1 $\mu$ W			15.5 - 17.2 $\mu$ W		
Measured power incl. biasing		37.1 $\mu$ W			18.9 $\mu$ W		

shows the case of cathodic first stimulation, exhibiting a 30% majority in negative charges, whereas  $P_2$  proves the concept in opposite direction, with a 30% majority in positive charges and anodic first stimulation. The black curve shows the case without CB. Remaining  $V_E$  of around  $\pm 2$  V is developed already after the first stimulus. Using IPCC,  $V_E$  is reduced into the safe window due to the autonomous supply of compensation current  $I_{IPCC}$ . The lower the current restrictions, the faster is the compensation. Once  $V_E$  enters the safe region, the IPCC turns inactive automatically. As a special feature, the IPCC can be used as a complement to monophasic stimulators.  $P_3$  of Fig. 9 shows the 100% stimuli mismatch compensation by autonomously generating the counter pulse of a monophasic stimulus.

### B. Characteristics of the PI-Controlled Offset Compensation

The presented cause-based CB method is shown in Fig. 5.  $V_E$  is monitored by the operational transconductance amplifier (OTA<sub>2</sub>) of the PI-controller, which then steers an LV OTA<sub>3</sub>. The resultant output current  $I_{OC}$  is directly added to the biasing current of the cathodic stimulation  $I_{DAC,c}$ , thus correcting the positive and negative stimulation intensities percentually.  $I_{OC}$  is designed for a maximum of  $\pm 40$  nA, compensating around  $\pm 36\%$  of charge mismatch in  $I_{DAC,c}$ . The PI-controller design is shown in Fig. 10. A common mode (CM) feedback (CMFB) differential difference amplifier (DDA) drives a part of the OTA<sub>2</sub> bottom current source, whereas the other part consists of a current source with a constant bias plus a 7-bit current DAC ( $I_{DAC}$ ) for offset adjustments. The CMFB is further used to shift the output level of OTA<sub>2</sub> from the HV environment into the LV (3 V) domain, reducing the power consumption of OTA<sub>3</sub> (Table I).

To monitor low-frequency bio signals, a large time constant  $\tau$  in the millisecond range is necessary [25], [27]. To meet this requirement for an on-chip implementation, with a reasonable small integration capacitance  $C_{int}$ , a very small  $G_m$  in the nS range is required. Hence, a cross coupling technique is implemented, in which  $G_m$  equals the difference in transconductance of the input stages M<sub>1,2</sub> (Fig. 10). This method allows for an improved linearity, since the third-order distortion of  $I_{int}$ , which corresponds to the second-order distortion of  $G_m$ , can be canceled [25]. The overall  $G_m$  is measured to be 1.5 nS only (Fig. 11), resulting in  $\tau$  of 8 ms, at a reasonable small  $C_{int}$  of 12 pF.



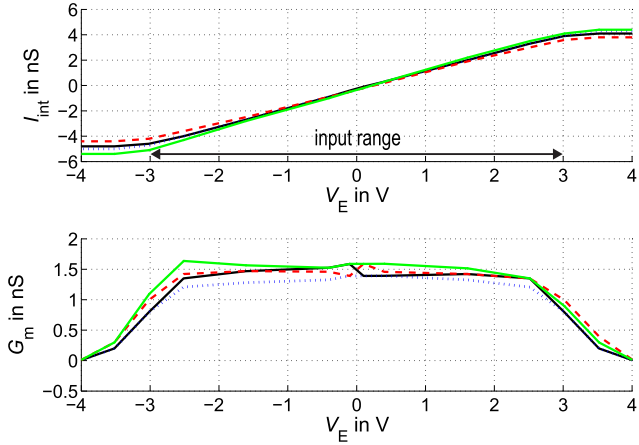


Fig. 11. Characteristics of the overall transconductance  $G_m$  and output current  $I_{\text{int}}$  of OTA<sub>2</sub>, measured for four chips.

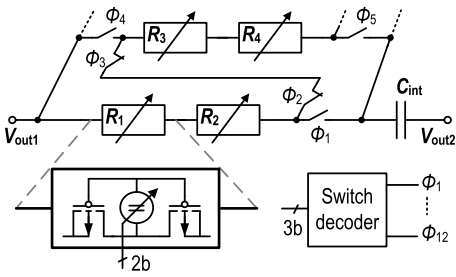


Fig. 12. Schematic of  $R_{\text{CMOS}}$  implementation.

parameters and applications. This is reached by on-chip trimming of the pseudo back-to-back CMOS resistor  $R_{\text{CMOS}}$ . As shown in Fig. 12,  $R_{\text{CMOS}}$  is realized by a switchable array of unit resistances, consisting of two transistors in series with their gates connected and controlled by an intermediate configurable voltage. In total, the resistor's value can be chosen from 0  $\Omega$  to 12 G $\Omega$  by five bits.

The measured results of the OC system, for a biphasic stimulation mismatch of 20%, are shown in Fig. 13. Without CB (black line),  $V_E$  increases with every stimulation pulse until it reaches a static state, at which the electrode self-discharge equals the stimulus mismatch charge. Thus, the electrode-tissue interface is permanently exposed to a harmful DC potential of around 10 V. Using OC, it is possible to control  $V_E$  by adjusting the cathodic stimulus amplitude. The second zoom compared with the first zoom of  $I_E$  shows that the current mismatch is being eliminated for both controllers. Once  $V_E$  has settled, the remaining  $V_E$  value of around  $\pm 20$  mV was measured, which is significantly smaller than the safety window of  $\pm 50$  or  $\pm 100$  mV.

### C. Closed-Loop Stability Considerations

Both CB implementations represent feedback control loops. The IPCC represents a P-control with inherent hysteresis for safety window detection, which introduces a dead zone around the target value. In contrast to digital implementations, where the stability depends on the individual and discrete charge packets, the continuous operation with decreasing

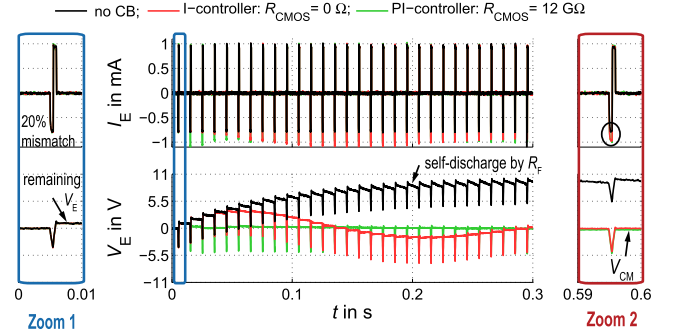


Fig. 13. Measured system result of the PI-controlled OC, compared with a non-balanced condition and an I-controlled OC using an electrode equivalent model with  $C_H$  of 0.1  $\mu$ F,  $R_F$  of 1 M $\Omega$ , and  $R_S$  of 1 k $\Omega$ .

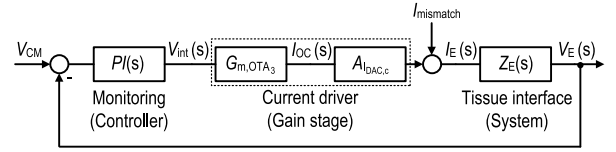


Fig. 14. PI-controlled OC in its standard control representation.

compensation amplitude for decreasing remaining  $V_E$  provides a smooth transition into the safety window. It thus makes overshoots impossible and provides inherent stability. Besides parasitics, the frequency response is mainly shaped by the pole  $p_E$  and zero  $z_E$  of the electrode. The controllers gain changes during operation, outside the dead zone, depending on the actual working point. The phase margin (PM) of the IPCC for its complete dynamic range (Fig. 8) is between 95° and 126°, which is simulated at  $C_H$  of 0.1  $\mu$ F,  $R_S$  of 1 k $\Omega$ , and  $R_F$  of 1 M $\Omega$ .

The presented PI-controlled OC method can be converted into the standard control representation, shown in Fig. 14. The controller of the loop is  $PI(s)$  with voltage output  $V_{\text{int}}$ , followed by a transconductance gain stage (considered as ideal), consisting of the  $G_m$  of OTA<sub>3</sub> and an additional gain  $A_{\text{DAC},c}$ , which is dependent on the setting of the cathodic  $I_{\text{DAC},c}$ . The system is defined by the electrode-tissue interface  $Z_E(s)$ . Via a direct feedback path,  $V_E$  is subtracted from the target value, which is the body's quiescent potential  $V_{\text{CM}}$ .

A non-ideal I-controller (PT-controller), as proposed in [9] and [25], is compared with the recommended non-ideal PI-controller  $PI(s)$  (Fig. 15). Their finite output resistance  $r_{\text{out}}$  introduces a low-frequency pole  $p_{\text{out}}$ . A non-ideal I-controller represents a one-pole system [25], whereas

$$PI(s) = \frac{r_{\text{out}}G_m \cdot (1 + sC_{\text{int}}R_{\text{CMOS}})}{1 + sC_{\text{int}}r_{\text{out}}} \quad (7)$$

does provide an additional zero  $z_{\text{PI}}$ , adding a further degree of freedom for stability adjustments by means of pole-zero compensation. For frequencies larger than  $p_{\text{out}}$ , the magnitude drops with 20 dB/decade, equivalent to an ideal integration behavior. The time constant for both controllers is defined by  $\tau = C_{\text{int}}/G_m$ .

For stability considerations, the open-loop characteristic of the control shown in Fig. 14 is examined. The transfer function

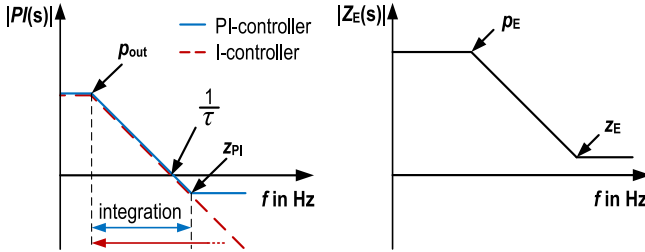


Fig. 15. Illustration of the magnitude of the non-ideal  $P_I(s)$  and  $I(s)$  transfer function (left) and electrode impedance  $Z_E(s)$  (right).

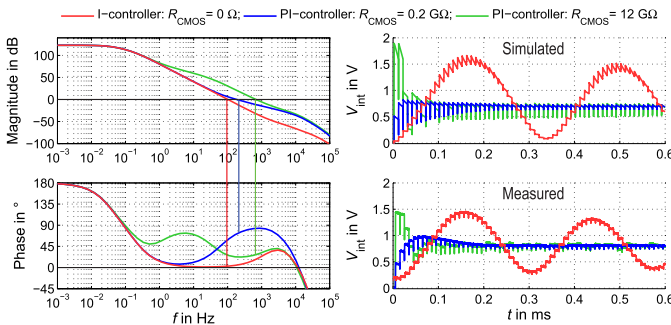


Fig. 16. Simulated bode plot of the PI-controlled OC in its open-loop configuration (left) for different  $R_{CMOS}$  settings and the corresponding simulated transient response of the closed-loop system (top right), which is compared with the measurement results (bottom right) for an electrode equivalent model with  $C_H$  of  $0.1 \mu\text{F}$ ,  $R_F$  of  $10 \text{ M}\Omega$ , and  $R_S$  of  $1 \text{ k}\Omega$ .

TABLE II  
POLES AND ZEROS OF THE OPEN-LOOP PI-CONTROLLED OC SYSTEM

$p_{out}$	$p_E$	$z_{PI}$	$z_E$
$\frac{1}{C_{int} r_{out}}$	$\frac{1}{C_{int} R_F}$	$\frac{1}{C_{int} R_{CMOS}}$	$\frac{1}{C_H (R_S \parallel R_F)}$

$PI(s)$  is multiplied by the system's transfer function  $Z_E(s)$ , which adds the pole  $p_E$  (Fig. 15), defined by the electrode parameters  $C_H$  and  $R_F$  and the zero  $z_E$ , and mainly defined by  $C_H$  and  $R_S$ , since  $R_S$  is typically much smaller than  $R_F$  (Table II). These parameters differ between electrodes, and thus change the settling behavior, which demands for an adjustable control. The adjustability of the control is shown in Fig. 16 in form of a simulated bode plot and the corresponding simulated and measured transient response at the controller's output  $V_{int}$ . Additional poles due to parasitics within the circuit are visible at frequencies above 10 kHz within the bode plot. The red curve shows the case for an I-control, for which in the presented design (Fig. 10)  $R_{CMOS}$  is shorted. Since both poles  $p_{out}$  and  $p_E$  are close to each other, the PM results to  $3^\circ$  only, which causes large overshoots and long transient settling times. However, using the PI-control, the settling behavior can be optimized by changing the value of  $R_{CMOS}$ , thus moving  $z_{PI}$  and increasing the PM. With  $R_{CMOS}$  of  $200 \text{ M}\Omega$ , the PM results to  $71^\circ$  and a fast and smooth settling is found. It is expected that once a setting for an electrode *in vitro* is chosen, changes due to electrode variations after implementation, for example, due to tissue growth, will

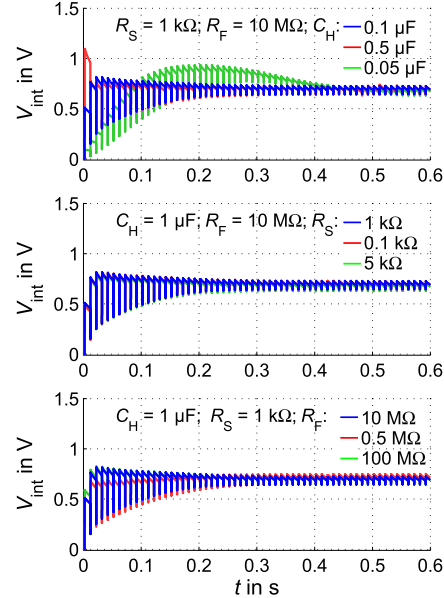


Fig. 17. Simulated behavior for the PI-controlled OC for changing electrode parameters based on the electrode equivalent model and recommended setting with  $R_{CMOS}$  of  $0.2 \text{ G}\Omega$  from Fig. 16.

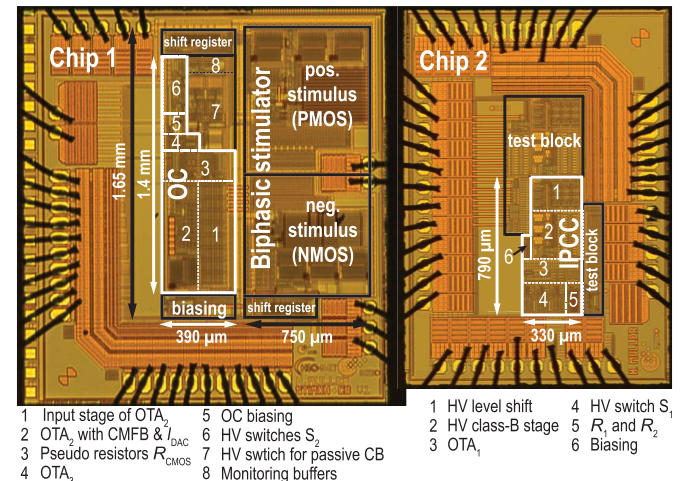


Fig. 18. Micrographs of Chip 1 consisting of the biphasic stimulator and the PI-controlled OC circuit and Chip 2 containing the IPCC.

not significantly influence the settling behavior of the system as shown in Fig. 17 and a recalibration is not needed.

## V. TWIN-TACK SYSTEM MEASUREMENT RESULTS

The IPCC and PI-controlled OC are fabricated separately to make use of the independence of the IPCC. Fig. 18 shows the chip micrographs: Chip 1 consists of the biphasic current-controlled stimulator and the PI-controlled OC circuit with  $1.23$  and  $0.45 \text{ mm}^2$  of die area, respectively, and Chip 2 contains the IPCC with  $0.26 \text{ mm}^2$ .

The IPCC and OC are combined to the Twin-Track system on PCB level (Fig. 19). The on-chip stimulator, capable of generating amplitudes from  $1 \mu\text{A}$  to  $5.12 \text{ mA}$  with 9-bit resolution, is controlled by an external FPGA. An intentional mismatch in cathodic and anodic stimuli is generated.  $S_1$  to  $S_3$

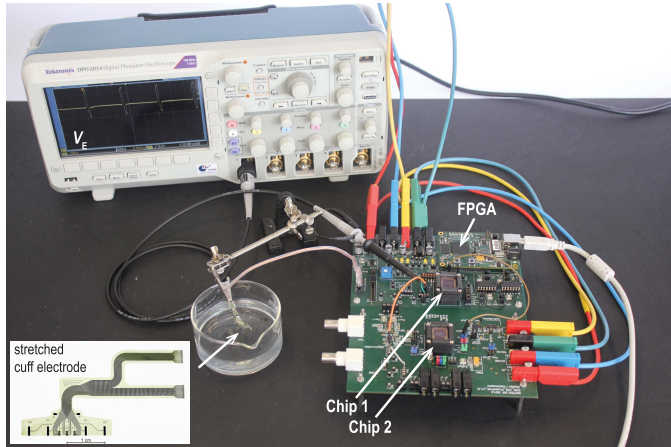


Fig. 19. Running *in vitro* measurement setup showing the polyimide thin-film cuff electrode in 0.9% saline solution and the PCB containing the two chips and the FPGA, providing the digital control signals.

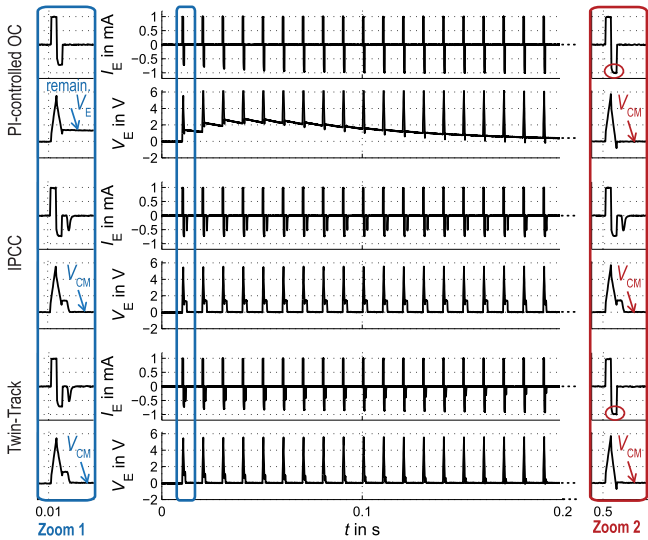


Fig. 20. Twin-Track measurement results for a biphasic stimulation pulse with the maximum of 36% mismatch, showing the control behavior of the PI-controlled OC, the IPCC, and their combination (Twin-Track).

are controlled by the FPGA with respect to the stimulation pulses according to the signal flow shown in Fig. 6. The system is measured with an electrode equivalent model as well as in an *in vitro* environment.

#### A. Twin-Track Measurement Results

The long-term impact of OC, IPCC, and their combination (Twin-Track), compensating a mismatch of 36%, is presented in Fig. 20. During the first stimulus, shown in zoom 1, the OC alone has not yet a charge balancing effect and, therefore,  $V_E$  exhibits an offset voltage. However, after some pulses, the system settles and  $V_E$  is kept at  $V_{CM}$ , reaching a long-term stable state by cathodic amplitude correction, as shown in zoom 2 at 0.5 s. While the OC demands an initial settling, the IPCC compensates remaining charges instantaneously from the first pulse on. Since the IPCC does not counteract the

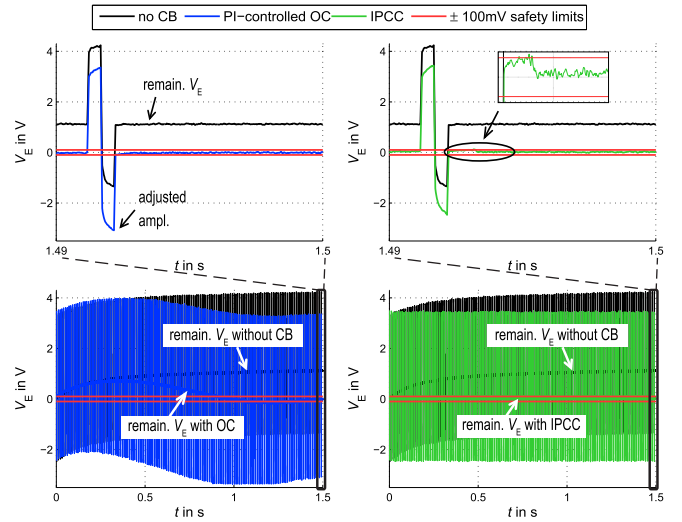


Fig. 21. *In vitro* measurement results with a polyimide thin-film cuff electrode in 0.9% saline solution for a biphasic stimulation pulse of 1 mA and 30% mismatch. Both graphs compare the imbalance stimulation condition (no CB) first with the settling behavior of the PI-controlled OC (left) and then with the IPCC's immediate and continuous charge compensation after each stimulus (right). The settled condition is shown for each graph by a zoomed-in view.

origin of the mismatch, it exhibits repeated activation over time. Consequently, the compensation response in the second stimulus is similar to the response to the first stimulus. When using both systems simultaneously, highest efficacy in terms of a charge balanced  $V_E$  is achieved. The IPCC is active only during the settling of the OC, with decreasing compensation intensities. As beneficial fail-safe backup, the IPCC would furthermore activate itself in the case of unforeseen voltage spikes, e.g., after nearby stimulation, or in the case of malfunction of the stimulus source. With the IPCC, an instantaneous charge compensation right from the first pulse on can be guaranteed, and additionally, a long-term stable state is reached by PI-controlled OC, equalizing the stimulation charges. The Twin-Track system consumes 56  $\mu$ W at 22 V.

#### B. In Vitro Measurement Results

The Twin-Track active charge balancer is tested in an *in vitro* environment with a polyimide thin-film cuff electrode [5] in 0.9% saline solution, shown in Fig. 19. A stimulation pulse of 1 mA with 30% mismatch is applied. The parameters for the provided electrode are found to be around  $C_H$  of 1.3  $\mu$ F,  $R_F$  of 100 k $\Omega$ , and  $R_S$  of 3 k $\Omega$  by applying the method of [28]. Without CB (no CB), the introduced mismatch will lead to a harmful permanent electrode potential of around 1.2 V (Fig. 21). However, using PI-controlled OC or IPCC,  $V_E$  is successfully kept within the safety window. The rather large capacitance  $C_H$  causes a slow rise of the resting potential, and thereby, results in a slow settling of the PI-controlled OC. Considering IPCC, compensation currents of about 40  $\mu$ A are sufficient to reduce  $V_E$  into the safety window. The *in vitro* results show that  $I_{IPCC}$  is not exploited to its maximum current limit for successful balancing. The measured  $I_{IPCC}$  compensation current yields 0.04% of the stimulation current only, thus not risking the nerve's restimulation.

TABLE III  
COMPARISON WITH THE STATE-OF-THE-ART CHARGE BALANCERS

Reference	[17]	[3]	[10]	[9]	[1]	<b>This work</b>
Process	0.13 $\mu\text{m}$	0.35 $\mu\text{m}$	0.5 $\mu\text{m}$	Discrete (PCB)	0.35 $\mu\text{m}$	0.35 $\mu\text{m}$
Max. $V_E$ compliance	3.3 V	4.2 V	4.6 V	30 V	20 V	22 V
Safety voltage detection	No control of $V_E$	No control of $V_E$	micro-controller	HV window comparator	HV window comparator	Intrinsic idle window
Safety window ( $\Delta V_{\text{safe}}$ )	N/A	N/A	$\pm 50 \text{ mV}$	$\pm 100 \text{ mV}$	$\pm 100 \text{ mV}$	$\pm 50 \text{ mV}$ or $\pm 100 \text{ mV}$
<b>Cause based CB methods</b>	Current matching	Charge monitoring	N/A	Analog OC	Digital OC	Analog OC
Precision	Stimulus mismatch $< 10 \text{ nA}$	Charge mismatch $< 22 \text{ nC}$	N/A	remaining $V_E < \Delta V_{\text{safe}}$	remaining $V_E < \Delta V_{\text{safe}}$	remaining $V_E \lesssim \pm 20 \text{ mV}$
Compensation range	N/A	N/A	N/A	N/A	$\pm 15\%$ of biphasic current	$\pm 36\%$ of biphasic current
Controller	S/H circuit	Zero crossing detection	N/A	Tunable I- or PT-controller ( $\tau = 4.7 \text{ ms}$ )	3-bit Moore state machine	Tunable I- or PI-controller ( $\tau = 8 \text{ ms}$ )
<b>Consequence based CB methods</b>	N/A	Passive CB	Short pulse injections	Short pulse injections	Short pulse injections	IPCC
Compensation currents	N/A	N/A	Fixed $\pm 20 \mu\text{A}$	Fixed $\pm 150 \mu\text{A}^1$	Fixed $\pm 100 \mu\text{A}^1$	Adjustable up to $\pm 500 \mu\text{A}$
Compensation time	N/A	N/A	20 $\mu\text{s}$ per spike	10 $\mu\text{s}$ per spike	25 $\mu\text{s}$ per spike	Self-adaptive

<sup>1)</sup>estimated

## VI. CONCLUSION

This paper presents a CMOS-integrated active charge balancer, accomplishing cause and consequence-based compensation, which is especially advantageous for achieving long-term stability with early tissue protection. The comparison of CB systems in Table III benchmarks the performance of the presented balancer against recently published systems. The HV compliance of this paper is 22 V, which is the highest reported compared with other integrated CB circuits.

Comparing cause-based methods, the publications [1], [9], as well as this paper, monitor  $V_E$ , thus responding to any kind of electrode–electrolyte voltage errors, in contrast to [3] and [17]. Compared with [9], the 1.5 nS transconductance presented in this paper enables an on-chip implementation of an analog PI-controlled OC, capable of up to  $\pm 36\%$  biphasic stimuli mismatch correction. The PI-control's system behavior is advantageous in terms of stability by means of pole-zero compensation, when compared with an I- or PT-control, since it offers one more degree of freedom to adapt to a wide variety of electrodes.

The consequence-based systems of previously published balancers use passive CB or short pulse injection. Compared with the latter, the IPCC provides continuous charge compensation with adjustable maximum current amplitudes, based on the real-time measurement of  $V_E$ . Furthermore, it provides inherent stability and avoids digital activity at the

tissue interface that may reduce the SNR of neural recording. By inherently incorporating hysteresis, the IPCC offers a self-regulated removal of charges for two configurable safety limits with adjustable maximum compensation currents. Additional components, such as control units or comparators, to define and detect the safety window are dispensable. It is the only known approach that is capable of replacing biphasic counter pulses with self-adaptive timing and without programming. In summary, the IPCC's simple methodology, low-current consumption of 1.22  $\mu\text{A}$ , and its ability to compensate a stimuli mismatch of up to  $\pm 100\%$  with respect to configurable safety windows, makes the IPCC suitable as independent standalone balancer, offering autonomous CB for arbitrary applications, e.g., steering currents, with even monophasic neural stimulators.

## ACKNOWLEDGMENT

The authors would like to thank Dr. Plachta from Neuroloop GmbH, Germany, for providing the electrode.

## REFERENCES

- [1] E. Noorsal, K. Sooksood, H. Xu, R. Hornig, J. Becker, and M. Ortmanns, "A neural stimulator frontend with high-voltage compliance and programmable pulse shape for epiretinal implants," *IEEE J. Solid-State Circuits*, vol. 47, no. 1, pp. 244–256, Jan. 2012.
- [2] M. Sivaprakasam, W. Liu, M. S. Humayun, and J. D. Weiland, "A variable range bi-phasic current stimulus driver circuitry for an implantable retinal prosthetic device," *IEEE J. Solid-State Circuits*, vol. 40, no. 3, pp. 763–771, Mar. 2005.

- [3] H.-M. Lee, K.-Y. Kwon, W. Li, and M. Ghovanloo, "A power-efficient switched-capacitor stimulating system for electrical/optical deep-brain stimulation," in *IEEE Int. Solid-State Circuits Conf. (ISSCC) Dig. Tech. Papers*, Feb. 2014, pp. 414–415.
- [4] D. T. T. Plachta, M. Gierthmuehlen, O. Cota, F. Boeser, and T. Stieglitz, "BaroLoop: Using a multichannel cuff electrode and selective stimulation to reduce blood pressure," in *Proc. IEEE Eng. Med. Biol. Soc.*, Jul. 2013, pp. 755–758.
- [5] D. T. T. Plachta *et al.*, "Blood pressure control with selective vagal nerve stimulation and minimal side effects," *J. Neural Eng.*, vol. 11, no. 3, p. 036011, May 2014.
- [6] O. F. Cota, D. T. T. Plachta, T. Stieglitz, Y. Manoli, and M. Kuhl, "In-vivo characterization of a 0.8 –3  $\mu$ VRMS input-noise versatile CMOS pre-amplifier," in *Proc. 7th Int. IEEE/EMBS Conf. Neural Eng.*, Apr. 2015, pp. 458–461.
- [7] J. Ai, R. D. Wurster, S. W. Harden, and Z. J. Cheng, "Vagal afferent innervation and remodeling in the aortic arch of young-adult fischer 344 rats following chronic intermittent hypoxia," *Neuroscience*, vol. 164, no. 2, pp. 658–666, Dec. 2009.
- [8] D. T. T. Plachta, J. Sonnenfeld, O. Cota, and T. Stieglitz, "A virtual workbench for peripheral electrode design," *VDI Automed.*, vol. 17, no. 286, pp. 61–63, 2012.
- [9] K. Sooksood, T. Stieglitz, and M. Ortmanns, "An active approach for charge balancing in functional electrical stimulation," *IEEE Trans. Biomed. Circuits Syst.*, vol. 4, no. 3, pp. 162–170, Jun. 2010.
- [10] H. M. Lee, H. Park, and M. Ghovanloo, "A power-efficient wireless system with adaptive supply control for deep brain stimulation," *IEEE J. Solid-State Circuits*, vol. 48, no. 9, pp. 2203–2216, Sep. 2013.
- [11] L. Yao and M. Je, "CMOS based 16-channel neural/muscular stimulation system with arbitrary waveform and active charge balancing circuit," in *Proc. IEEE Int. Symp. Integr. Circuits*, Dec. 2011, pp. 456–459.
- [12] M. Ghovanloo, "Switched-capacitor based implantable low-power wireless microstimulating systems," in *Proc. IEEE Int. Symp. Circuits Syst.*, May 2006, pp. 2197–2200.
- [13] A. Wongsarnpigoon, J. P. Wock, and W. M. Grill, "Efficiency analysis of waveform shape for electrical excitation of nerve fibers," *IEEE Trans. Neural Syst. Rehabil. Eng.*, vol. 18, no. 3, pp. 319–328, Jun. 2010.
- [14] M. Ortmanns, "Charge balancing in functional electrical stimulators: A comparative study," in *Proc. IEEE Int. Symp. Circuits Syst.*, May 2007, pp. 573–576.
- [15] D. R. Merrill, "The electrochemistry of charge injection at the electrode/tissue interface," in *Implantable Neural Prostheses: Techniques and Engineering Approaches*. New York, NY, USA: Springer, 2010, pp. 85–138.
- [16] J.-J. Sit and R. Sarapeshkar, "A low-power blocking-capacitor-free charge-balanced electrode-stimulator chip with less than 6 nA DC error for 1-mA full-scale stimulation," *IEEE Trans. Biomed. Circuits Syst.*, vol. 1, no. 3, pp. 172–183, Sep. 2007.
- [17] K. Song, H. Lee, S. Hong, H. Cho, and H.-J. Yoo, "A sub-10 nA DC-balanced adaptive stimulator IC with multimodal sensor for compact electro-acupuncture system," in *IEEE Int. Solid-State Circuits Conf. (ISSCC) Dig. Tech. Papers*, Feb. 2012, pp. 296–298.
- [18] J. J. Wheeler *et al.*, "An implantable 64-channel neural interface with reconfigurable recording and stimulation," in *Proc. 37th Annu. Int. Conf. IEEE Eng. Med. Biol. Soc.*, Aug. 2015, pp. 7837–7840.
- [19] X. Liu, A. Demosthenous, and N. Donaldson, "An integrated implantable stimulator that is fail-safe without off-chip blocking-capacitors," *IEEE Trans. Biomed. Circuits Syst.*, vol. 2, no. 3, pp. 231–244, Sep. 2008.
- [20] R. K. Shepherd, N. Linahan, G. Xu, and S. Araki, "Chronic electrical stimulation of the auditory nerve using non-charge-balanced stimuli," *Acta Oto-Laryngol.*, vol. 119, no. 6, pp. 674–684, 1999.
- [21] Y.-K. Lo, R. Hill, K. Chen, and W. Liu, "Precision control of pulse widths for charge balancing in functional electrical stimulation," in *Proc. 6th Int. IEEE/EMBS Conf. IEEE Neural Eng.*, Nov. 2013, pp. 1481–1484.
- [22] L. Yao, P. Li, and M. Je, "A pulse-width-adaptive active charge balancing circuit with pulse-insertion based residual charge compensation and quantization for electrical stimulation applications," in *Proc. IEEE Asian Solid-State Circuits Conf.*, Nov. 2015, pp. 1–4.
- [23] H. Chun, Y. Yang, and T. Lehmann, "Safety ensuring retinal prosthesis with precise charge balance and low power consumption," *IEEE Trans. Biomed. Circuits Syst.*, vol. 8, no. 1, pp. 108–118, Feb. 2014.
- [24] N. Butz, A. Taschwer, Y. Manoli, and M. Kuhl, "A 22V compliant 56  $\mu$ W active charge balancer enabling 100% charge compensation even in monophasic and 36% amplitude correction in biphasic neural stimulators," in *IEEE Int. Solid-State Circuits Conf. (ISSCC) Dig. Tech. Papers*, Jan./Feb. 2016, pp. 390–391.
- [25] N. Müller, Y. Manoli, and M. Kuhl, "A 1.6 nS, 16  $\mu$ W, 30 V Gm-C integrator for offset voltage monitoring in neural stimulators," in *Proc. IEEE Int. Symp. Circuits Syst.*, Jun. 2014, pp. 2381–2384.
- [26] D. R. Merrill, M. Bikson, and J. G. R. Jefferys, "Electrical stimulation of excitable tissue: Design of efficacious and safe protocols," *J. Neurosci. Methods*, vol. 141, no. 2, pp. 171–198, 2005.
- [27] A. Veeravalli, E. Sanchez-Sinencio, and J. Silva-Martinez, "Transconductance amplifier structures with very small transconductances: A comparative design approach," *IEEE J. Solid-State Circuits*, vol. 37, no. 6, pp. 770–775, Jun. 2002.
- [28] Y.-K. Lo *et al.*, "A 176-channel 0.5 cm<sup>3</sup> 0.7G wireless implant for motor function recovery after spinal cord injury," in *IEEE Int. Solid-State Circuits Conf. (ISSCC) Dig. Tech. Papers*, Jan./Feb. 2016, pp. 382–383.



**Natalie Butz** (S'14) received the B.Eng. degree in biomedical engineering from the University of Applied Sciences Ulm, Ulm, Germany in 2010, and the M.Sc. degree in microsystems engineering from the University of Freiburg, Freiburg, Germany, in 2012, where she is currently pursuing the Ph.D. degree with the Fritz Huettinger Chair of Microelectronics, Department of Microsystems Engineering (IMTEK), under the supervision of Prof. Y. Manoli.

Her current research interest includes the field of low-power analog circuits for biomedical application.



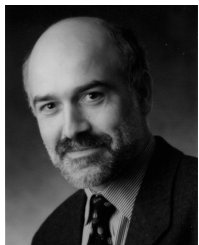
**Armin Taschwer** (M'09) received the Dipl.-Ing. degree from the Graz University of Technology, Graz, Austria, in 2004.

From 2004 to 2006, he was with Philips Semiconductors (now NXP), Gratkorn, Austria, he worked on low-power analog-to-digital converters. Since 2006, he is working in Freiburg, Germany. First, he was with IMTEK, Germany, and since 2008, he has been a Research Assistant with Hahn-Schickard, Villingen-Schwenningen, Germany. His current research interest includes low-power mixed signal integrated circuits for various applications around biological and sensor interfaces.



**Sebastian Nessler** (S'15) received the B.Sc. and M.Sc. degrees in microsystems engineering from the University of Freiburg, Freiburg, Germany, in 2010 and 2013, respectively, where he is currently pursuing the Ph.D. degree, under the supervision of Prof. Y. Manoli.

Since 2013, he has been with the Fritz Huettinger Chair of Microelectronics, Department of Microsystems Engineering (IMTEK), University of Freiburg. His current research interest includes closed-loop sensor read out and the design of low-power interface electronics for capacitive microelectromechanical sensors.



**Yiannos Manoli** (M'82–SM'08) was born in Famagusta, Cyprus, in 1954. He received the B.A. degree (*summa cum laude*) in physics and mathematics from Lawrence University in Appleton, WI, USA; in 1978, the M.S. degree in electrical engineering and computer science from the University of California, Berkeley, CA, USA, in 1980, both on a Fulbright scholarship, and the Dr.-Ing. degree in electrical engineering from the Gerhard Mercator University, Duisburg, Germany, in 1987.

From 1980 to 1984, he was a Research Assistant at the University of Dortmund, Dortmund, Germany, in the field of A/D and D/A converters. In 1985, he joined the newly founded Fraunhofer Institute of Microelectronic Circuits and Systems, Duisburg, Germany, where he established a design group working on mixed-signal CMOS circuits especially for monolithic integrated sensors and application specific microcontrollers. From 1996 to 2001, he held the Chair of Microelectronics as full professor with the Department of Electrical Engineering, University of Saarland, Saarbrücken, Germany.

In 2001, he joined the Department of Microsystems Engineering (IMTEK) in the Faculty of Engineering, University of Freiburg, Freiburg, Germany where he established the Chair of Microelectronics. In memory of the founder of today's Trumpf Hüttlinger GmbH, this chair was endowed by the Fritz Hüttlinger Foundation in 2010 and has since carried the name Fritz Hüttlinger Chair of Microelectronics". From 2008 until 2015 Professor Manoli served as Associate Dean and as Dean of the Faculty of Engineering.

Together with his colleague Roland Zengerle, he has been director of the "Hahn-Schickard-Institut für Mikro- und Informationstechnik" in Villingen-Schwenningen and Freiburg, Germany since 2005.

His current research interests are the design of low-voltage/low-power mixed-signal CMOS circuits, energy harvesting electronics, sensor read-out circuits as well as Analog-to-Digital converters. Additional research activities concentrate on motion and vibration energy transducers as well as on inertial sensors and sensor fusion.

In 2000, he had the opportunity to spend half a year on a research project with the Sensor Division of Motorola in Phoenix, AZ, USA. Yiannos Manoli spent a semester, with Intel, Santa Clara, CA, USA, in 2006 working on the high-resolution read-out electronics for a wide-bandwidth accelerometer. A sabbatical leave at Columbia University in New York in 2017 has led to a creative and productive collaboration in the area of biomedical applications. He is among the first group of five fellows that were awarded a Thomas Mann Fellowship in Los Angeles in 2018.

Prof. Manoli and his group have received best paper awards at ESSCIRC 1988, 2009 and 2012, PowerMEMS 2006, MWSCAS 2007, and MSE-2007. The MSE-2007 award was granted for SpicyVOLTsim ([www.imtek.de/svs](http://www.imtek.de/svs)),

a web-based application for the animation and visualization of analog circuits for which Yiannos Manoli also received the Media Prize of the University of Freiburg in 2005. Further developments of SpicyVOLTsim were supported with a "Fellowship for Innovations in University Teaching" of the Baden-Württemberg Foundation in 2011. He was the first to receive the Best Teaching Award of the Faculty of Engineering when it was introduced in 2008. For his creative contributions to an interactive teaching of microelectronics, he has also received the Excellence in Teaching Award of the University of Freiburg and the Teaching Award of the State of Baden-Württemberg, both in 2010.

Professor Manoli has served as a Distinguished Lecturer of the IEEE and on the Senior Editorial Board of the IEEE JOURNAL ON EMERGING AND SELECTED TOPICS IN CIRCUITS AND SYSTEMS and in addition as guest editor of the IEEE TRANSACTIONS ON VERY LARGE-SCALE INTEGRATION (VLSI) SYSTEMS and the IEEE JOURNAL OF SOLID-STATE CIRCUITS. He is on the Editorial Board of the *Journal of Low Power Electronics*. Yiannos Manoli has served on the committees of a number of conferences such as ISSCC, ESSCIRC, IEDM and ICCD, and was Program Chair (2001) and General Chair (2002) of the IEEE International Conference on Computer Design (ICCD). He is a member of VDE, Phi Beta Kappa, Mortar Board, and senior member of the IEEE.



**Matthias Kuhl** (M'07) received the B.Sc. and M.Sc. degrees in electrical engineering from the University of Wuppertal, Wuppertal, Germany, in 2004 and 2006, respectively, and the Ph.D. degree in microelectronics from the Fritz Hüttlinger Chair of Microelectronics, Department of Microsystems Engineering (IMTEK), University of Freiburg, in 2013.

From 2006 to 2018, he was with the Fritz Hüttlinger Chair of Microelectronics, Department of Microsystems Engineering (IMTEK), University of Freiburg, where he founded and has been leading the Medical Microelectronic Devices and Implantable Circuits Group, since 2013, and was appointed as a Junior Professor of integrated interface circuits in 2015. In 2018, he was appointed as a Full Professor with the Hamburg University of Technology, Germany, where he currently heads the Institute for Integrated Circuits. His current research interests include CMOS-integrated circuits for sensing applications and neural interfaces.

Dr. Kuhl is a member of VDE.